Construction and Building Materials 503 (2025) 144585

Contents lists available at ScienceDirect

Construction and Building Materials

journal homepage: www.elsevier.com/locate/conbuildmat

Compressive behaviour of mortar panels reinforced with polymeric auxetic lattices: Experimental testing and numerical modelling

Mohammad Hajsadeghi [a,b,*], Liyao Wan [b,**], Emmanuel O. Momoh [c], Amila Jayasinghe [d,e], Raffaele Vinai [b], Prakash Kripakaran [b], Ken E. Evans [b], John J. Orr [d]

[a] School of Science, Engineering and Environment, University of Salford, Manchester M5 4WT, UK
[b] Department of Engineering, University of Exeter, Exeter EX4 4QF, UK
[c] Department of Civil Engineering, University of Wolverhampton, Wolverhampton WV10 0JP, UK
[d] Department of Engineering, University of Cambridge, Cambridge CB3 0FA, UK
[e] School of Physics, Engineering and Computer Science, University of Hertfordshire, Hatfield AL10 9AB, UK

ARTICLE INFO

Keywords:
Reinforcing auxetic lattice
Cementitious material
3D printing
Numerical modelling

ABSTRACT

This paper examines the compressive performance of composite cement-based mortar panels embedding polymeric auxetic lattices, through both experimental testing and numerical modelling. In the experimental phase, lattices measuring 200 mm × 200 mm × 30 mm are fabricated using three-dimensional (3D) printing technology with Polyethylene Terephthalate Glycol (PETG) in four different auxetic geometries: re-entrant, tetra-anti-chiral, missing rib, and double arrowhead. Plain mortar specimens (panels) and those embedded with conventional non-auxetic honeycomb (hexagonal) lattices are prepared and tested to provide a comparative baseline against the mortar-filled auxetic lattices. The test results reveal that the auxetic reinforcing lattices significantly enhance the compressive characteristics of the mortar panels. On average, the peak load, toughness, and ductility ratio increase by 10 %, 1400 %, and 170 %, respectively; however, the initial stiffness is reduced by about 50 % compared to the plain mortar counterparts. A Finite Element (FE) model is developed and validated against the experimental data. The model is then employed as a virtual laboratory unit to investigate the performance of various Lattice-Reinforced Cementitious Composite (LRCC) panels with conventional construction materials (steel and normal-strength concrete).

1. Introduction

The term auxetic, introduced by Evans et al. in 1991 [1], refers to materials having a negative Poisson's ratio (NPR). These materials either contract or expand transversely when subjected to axial compression or tension respectively [2,3]. These materials offer several advantages, including lower densities due to their cellular structures, high resistance to shear and indentation, crashworthiness, energy absorption, damping capabilities, and enhanced acoustic properties. Additionally, auxetic materials naturally form synclastic curvature under bending moments and possess an intrinsic ability to decouple Young's modulus from shear modulus. These unique properties make them suitable for a wide range of applications, such as crash barriers, breakwaters, sandwich structures, filters, base isolation, blast shields, concrete reinforcement, seismic bracing elements, pipelines, domes, nails, and fasteners [3]. Furthermore, they show great potential in strengthening structures subjected to dynamic loads [2].

Cementitious materials are widely used in construction for their affordability and ease of production, which typically involves pouring the fluid material into moulds and allowing it to set [3,4]. Although these materials excel in compressive strength, they are unsuitable for high-energy absorption applications such as vibration and impact resistance due to their inherent brittleness and poor tensile strength. Various reinforcement techniques have therefore been explored to improve the tensile strength and/or ductility of these brittle materials, including the incorporation of reinforcing bars, strands, fibres, and, more recently, auxetic lattices [2,5–7].

A fair number of compression tests on three-dimensional-printed (3D-printed) auxetic space lattice-reinforced cementitious composites have been conducted by researchers. Salazar et al. [8] and Chen et al. [9] used polymeric 3D-printed lattices (octet-truss, re-entrant honeycomb,

* Corresponding author at: School of Science, Engineering and Environment, University of Salford, Manchester M5 4WT, UK.
** Corresponding author.
E-mail addresses: m.hajsadeghi@salford.ac.uk (M. Hajsadeghi), l.wan2@exeter.ac.uk (L. Wan).

https://doi.org/10.1016/j.conbuildmat.2025.144585
Received 10 April 2025; Received in revised form 5 September 2025; Accepted 18 November 2025
Available online 19 November 2025

Notations

a	Distance from the hydrostatic axis to the compression axis
b	Distance from the hydrostatic axis to the tension axis
B	Width of lattice cells (RE and DA)
d	Depth of lattice cells
d_n	Non-dimensional damage parameter
d_c	Damage parameter in uniaxial compression
d_t	Damage parameter in uniaxial tension
E	Young's modulus
E_o	Initial Young's modulus
f_c	Uniaxial compressive stress
f_{bo}	Biaxial compressive strength
f_{cu} - f_{co}	Uniaxial compressive strength
f_t	Uniaxial tensile stress
f_{to}	Uniaxial tensile stress at failure
f_{tu}	Uniaxial tensile strength
f_y	Yield stress of steel
f_X^D	Residual strength
G	Flow potential
H	Height of lattice cells (RE, TAC, MR, and DA)
K	Ratio of a over b
K_e	Initial stiffness
l	Length of lattice cell walls (TAC, MR, DA, and CH)
n	Calibration parameter
p	Hydrostatic pressure stress
P	Peak load
q	Mises equivalent effective stress
r	Radius of cylindrical core of lattice cells (TAC)
t	Thickness of lattice cells
T_X^D	Toughness
δ_P	Vertical displacement at the peak load
ε	Total strain
ε_c	Compressive strain
ε_{cr}	Cracking strain
ε_{cu}	Ultimate compressive strain
ε_t	Tensile strain
ε^{pl}	Plastic strain
$\varepsilon_o{}'$	Strain at the peak stress
θ	Acute angle between the lattice cell walls (RE, TAC, and DA)
μ	Ductility ratio
μ_f	Coefficient of friction
ν	Poisson's ratio
σ	Cauchy stress
$\emptyset$	Obtuse angle between the lattice cell walls (MR and DA)
ψ	Dilation angle
ϵ	Eccentricity parameter

and re-entrant triangular) to reinforce Ultra-High-Performance Concrete (UHPC). The results indicated that the confinement effect of the auxetic lattices can greatly enhance the mechanical properties (compressive strength and toughness) and ductility of UHPC. Hao et al. [10] examined various complex polymeric lattice structures for use as reinforcement for cement-based normal strength materials. The findings revealed that the printed lattices can significantly enhance the mechanical properties and failure mechanisms of the materials under uniaxial compression. Tzortzinis et al. [11] employed Direct Metal Laser Sintering (DMLS) technology to fabricate reinforcing steel lattices. Consistent with previous research findings, the results demonstrated that the confinement provided by the steel lattices notably enhances the strength and ductility of cementitious materials under pure compression.

Salazar et al. [8] also conducted flexural tests on polymeric 3D-printed space lattice-reinforced UHPC prisms. The results demonstrated that embedding the lattice structures in UHPC effectively enhances its ductility, exhibiting deflection-hardening behaviour. Zhong et al. [12] conducted a parametric study on the compressive performance of planar auxetic steel re-entrant honeycombs filled with concrete, investigating parameters such as cell wall thickness and cell angle. Their results revealed that increasing the cell wall thickness and angle enhances the energy absorption capacity and initial peak stress of the composite panels. Zhou et al. [13] examined the behaviour of foam concrete-filled auxetic aluminium honeycomb panels under quasi-static and dynamic compression through experimental testing and numerical analyses. The study showed that as the density of the foam concrete increases, the failure mode of the specimens shifts from compression failure, characterised by low peak stress and stable plateau stress, to shear failure, marked by high peak stress and significantly fluctuating plateau stress. As the compression loading rate increases, the response of the specimen transitions from quasi-static to dynamic mode, leading to localised crushing near the loading end and a reduction in the effective Poisson's ratio of the composites.

Choudhry et al. [14] examined the compressive behaviour of cementitious panels reinforced with various polymeric 3D-printed planar auxetic lattice designs. The findings show that embedding the lattice reinforcement in the panels significantly enhances their peak stress, ductility, Young's modulus, and energy absorption capacity. Moreover, these properties can be further tailored by adjusting the lattice's geometrical parameters. Vitalis et al. [15] examined mortar composites reinforced with stainless-steel 3D auxetic truss lattices (double-pyramid and bowtie geometries), forming an interpenetrating lattice-mortar system. Under quasi-static uniaxial compression, auxetic confinement increases effective confining pressure and, relative to unreinforced mortar, enhances peak strength and ductility. Numerical modelling reproduces the compression response and attributes the gains to auxetic lateral contraction and a bending-to-stretching transition in the lattice.

Previous studies on the compressive behaviour of auxetic lattice-reinforced cementitious composites have predominantly focused on re-entrant honeycomb geometries, using either polymeric 3D-printed lattices or folded-and-welded steel lattices. While these works demonstrate clear benefits in ductility, energy absorption, and post-peak behaviour, research on alternative auxetic geometries such as missing rib and double arrowhead is emerging but remains comparatively underexplored. This underscores the need to examine whether such alternatives can offer comparable or enhanced performance, thereby broadening the design space for future lattice-reinforced cementitious composites.

This study presents a systematic comparison of several under-explored auxetic lattice configurations (tetra-anti-chiral, missing rib, and double arrowhead) alongside the well-studied re-entrant geometry. Steel auxetic lattices can be produced using techniques such as bending and welding, casting, and metal powder bed fusion. The bending-and-welding method is labour-intensive and becomes increasingly complex for intricate geometries, with only simpler patterns like the re-entrant design being relatively feasible. Casting can be limited by mould complexity, surface finish requirements, and the risk of defects in thin lattice walls. Metal powder bed fusion can produce highly accurate and complex lattices, but at a very high cost. Considering these challenges in manufacturing complex auxetic lattice structures using steel, this study aims, as a first step, to cost-effectively and efficiently assess the potential benefits of the under-explored auxetic geometries manufactured using polymeric materials. Promising results can then enable follow up investigations with fabricated metallic lattices. The lattices in this study are fabricated from PETG polymer via Fused Deposition Modelling (FDM).

Given PETG's lower tensile strength compared to steel, a low-strength cementitious material is used as the filling medium. The study includes panels with no auxetic lattice embedded (plain mortar panels) and those reinforced with conventional non-auxetic honeycomb lattices for reference.

A Finite Element (FE) model is developed and validated against experimental data, serving as a virtual laboratory unit to investigate the behaviour of various Lattice-Reinforced Cementitious Composite (LRCC) panels using conventional construction materials (steel and normal-strength concrete).

2. Experimental programme

Cementitious materials exhibit inherent variability in mechanical properties. Therefore, in the experimental testing of mortar-filled specimens, six specimens are cast and tested for each configuration, with outliers removed based on deviation from the median response. To ensure consistency, three representative specimens are ultimately retained, with mean values used to characterise the overall behaviour.

2.1. Fabrication of lattices

The lattices are additively manufactured using a commercial Fused Deposition Modelling (FDM) 3D printer (Bambu X1-Carbon). Additive manufacturing allows the direct creation of 3D objects from digital models by depositing successive lines and layers of polymers, ceramics, or metals. The lattices measure 200 mm × 200 mm × 30 mm and are printed in five different patterns: re-entrant, tetra-anti-chiral, missing rib, double arrowhead, and conventional honeycomb, as shown in Fig. 1.

A recent study indicated that re-entrant angles (θ) in the range of 50–56° achieve an optimum balance between auxetic response, in-plane stiffness, and stable synclastic deformation [16]. In this study, an angle of 53° is considered for the angle, lying within this optimum range. Basic simulations are also performed to assess the influence of reinforcement ratio, showing that a value of approximately 15 % is required for the lattice to provide a clear contribution to the post-peak response of the panels. Prior fabrication experience shows that 0.75 mm is the minimum wall thickness achievable without defects. To maintain the reinforcement ratio of 15 % while considering the lower thickness limit, the wall thickness is set to 0.89 mm, resulting in a cell width (B) of 21.78 mm and a cell height (H) of 20.89 mm. For the other lattice structures, cell sizes are kept comparable to the re-entrant geometry, with wall thicknesses adjusted (subject to the 0.75 mm limit) to preserve the 15 % reinforcement ratio and to accommodate an integer number of cells within the lattice size.

The geometrical properties of the constituent cells for the different patterns are provided in Table 1. These values are taken directly from the digital models, with as-built measurements confirming deviations within ±0.1 mm.

All the wall thicknesses are small relative to the other dimensions, as is the lattice's depth compared to their height and width; therefore, the lattices can be regarded as thin-walled structures. The lattices are 3D printed using PETG polymer as it possesses low shrinkage rates, satisfactory strength, and flexibility compared to other polymeric materials. Besides, it prints easily with excellent layer adhesion, ensuring that the intricate lattice structures are formed accurately with minimal print

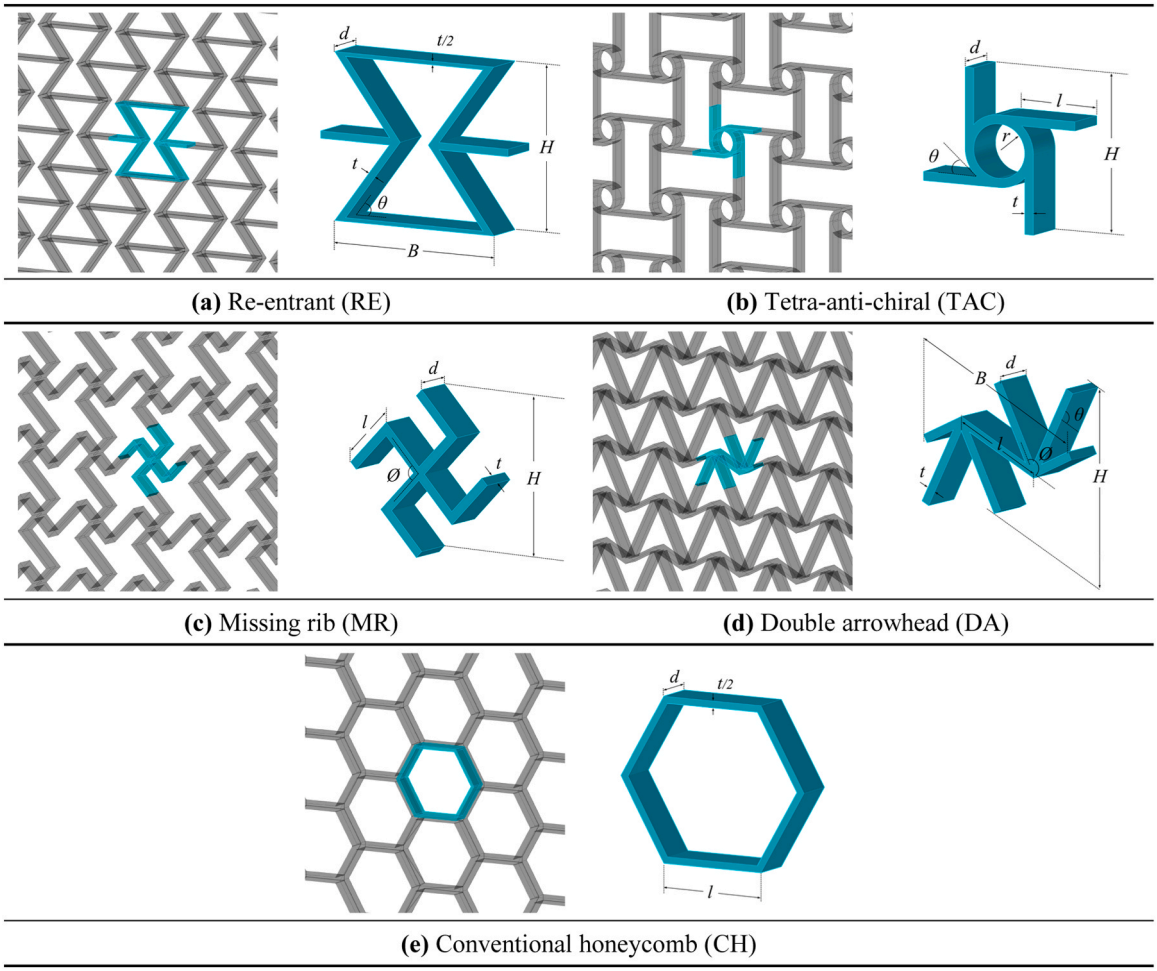

Fig. 1. Lattice structures with corresponding geometrical parameters indicated.

Table 1
Geometrical properties of lattice structures (described in the notation table).

Parameters	B (mm)	H (mm)	l (mm)	d (mm)	r (mm)	t (mm)	θ (°)	$\emptyset$ (°)
Re-entrant	21.78	20.89	-	30	-	0.89	53	-
Tetra-anti-chiral	-	20	10	30	3.375	1.125	41	-
Missing rib	-	20	7.65	30	-	1.16	-	90
Double arrowhead	20	15	10	30	-	0.77	63	143
Conventional honeycomb	-	-	13.6	30	-	1.65	-	-

failures. PETG filament (1.75 mm diameter) is extruded through a 0.4 mm diameter nozzle to fabricate the lattices using a layer-by-layer deposition technique. The X and Y directions are selected as the printing directions, while the Z direction is set as the build direction, see Fig. 2 [17]. The deposition of side-by-side PETG lines extruded along the walls' direction forms the thickness of the solid walls, rendering the raster angle irrelevant in this context [18]. Other printing parameters are summarised in Table 2.

Table 2
Fused deposition modelling (FDM) 3D printer parameters.

Printing speed (mm/s)	Layer thickness (mm)	Infill density (%)	Extruder temperature (°C)	Bed temperature (°C)
250	0.2	100	255	70

2.2. Properties of printed PETG lattices

The PETG used in this research is an isotropic material and has a nominal ultimate strength of 45 MPa. The additive manufacturing technique (3D printing) used to fabricate the lattices however results in anisotropy in the printed material. To assess the mechanical properties of the printed material, dog-bone shaped specimens conforming to ISO 527-1BA [19] (see Fig. 3**(a)**) are printed, using the same printing parameters as those for the lattices. Tensile testing is performed using a Shimadzu AGS-X 20 kN UTM, equipped with a Digital Image Correlation (DIC) system that includes a camera to accurately measure displacement and strain (see Fig. 3**(b)**). As seen in Fig. 3**(a)**, two sets of dog-bone specimens are assessed: in the first set (RA90), the extruded molten filaments are deposited longitudinally along the sample (raster angle of 90°), and in the second set (RA0), they are deposited transversely (raster angle of 0°). For each set, three identical samples are tested, and the mean results are considered as the representative behaviour of the corresponding set. These configurations, in turn, yield the ultimate tensile strength of the printed PETG and the ultimate bond strength between the print layers, which are found to be 43.5 MPa and 30.8 MPa, respectively, as illustrated in Fig. 3**(c)**. The Young's modulus derived from the RA90 and RA0 specimens is 1.900×10^3 MPa and 1.875×10^3 MPa, respectively, calculated from high-frequency (100 Hz) noise-reduced data using a moving average in the 0.05–0.25 % strain range, where the specimens exhibit linear behaviour. For presentation in Fig. 3**(c)**, the data are downsampled for clarity without affecting the calculated values. These results are aligned with the datasheet provided by the supplier of PETG.

The Poisson's ratio of the auxetic lattices is determined from compression tests conducted using an Instron 5900 Series 50 kN universal testing machine, where the longitudinal and in-plane transverse strains are measured using the DIC technique. The DIC analysis is performed on images captured with a GoPro Hero 12 camera and later processed with open-source software. Fig. 4**(a)** shows the tetra-anti-chiral lattice under compression at vertical displacement of 10 mm and 25 mm. Fig. 4**(b)** presents the variation of Poisson's ratio with vertical displacement for the auxetic lattices, while Fig. 4**(c)** shows the corresponding load-displacement responses.

The Poisson's ratios are computed at discrete displacement intervals of 1 mm, as indicated by the markers in the figure. The data points are interpolated under the assumption of linear variation between successive increments, with straight lines connecting the markers to represent this relationship. The DIC targets are placed symmetrically within the panels' cores (25–50 % of the span) to reduce potential boundary effects, with two sets in each direction (horizontal and vertical): one positioned closer to the mid-span and the other further away. Poisson's ratios are calculated separately from the closer and further target sets and subsequently averaged to minimise variability and yield more representative values.

2.3. Properties of cementitious mortar

To account for the relatively low stiffness of the polymeric lattices, the mortar is designed and tested on three 50 mm cube specimens at 28 days, yielding a compressive strength of approximately 6 MPa and a modulus of elasticity of about 3.2 GPa. For each litre of mortar, 200 g of Type III Ordinary Portland Cement (OPC), 300 g of fine crushed tile powder, and 1375 g of fine sand with a maximum particle size of 1 mm are combined and dry-mixed for approximately two minutes using a drum mixer. A lignosulfonate-based superplasticiser, dosed at 1 % of the

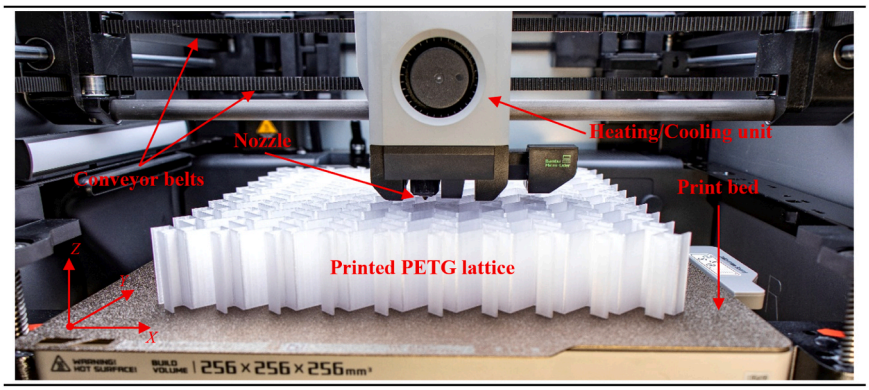

Fig. 2. Representation of lattice 3D printing (Z build direction).

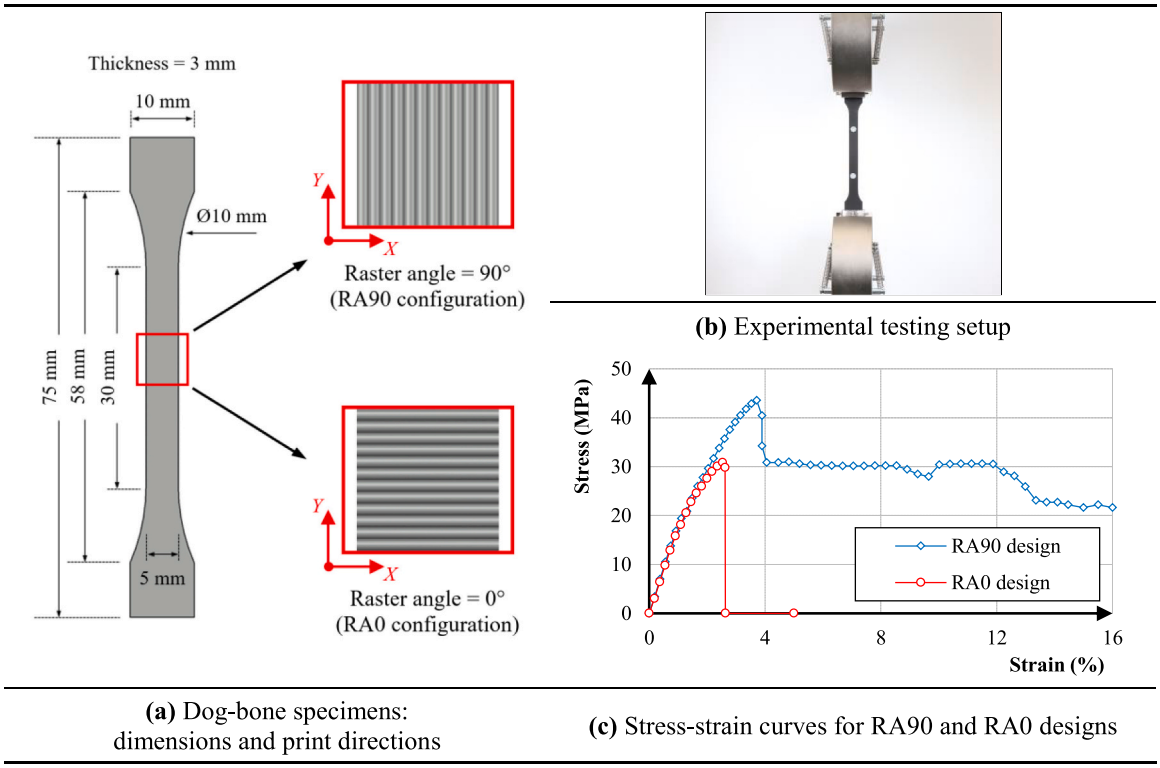

Fig. 3. Tensile characterisation of printed PETG.

cement content and mixed with 300 g of water, is subsequently added to the dry mixture, followed by an additional mixing period of five minutes.

2.4. Preparation of specimens – casting, curing, and testing

The LRCC specimens are prepared by pouring Portland cement-based mortar into moulds where lattices are laid. The fabrication steps for the panel composites are summarised in Fig. 5.

Custom-sized moulds, with internal dimensions matching those of the lattices (200 mm × 200 mm × 30 mm), are 3D printed using Carbon Fibre reinforced Polylactic Acid (PLA-CF) material. Then the LRCC panels are de-moulded the day after casting and cured for 28 days in a moist environment chamber. Unreinforced panels, which do not contain embedded lattices, are prepared following the same procedure. The LRCC panels, featuring five lattice designs (re-entrant, tetra-anti-chiral, missing rib, double arrowhead, and conventional hexagonal honeycomb) are labelled LRCC-R, LRCC-T, LRCC-M, LRCC-D, and LRCC-C respectively. The panels with auxetic lattices are collectively referred as A-LRCC. Six specimens for each configuration of panels (unreinforced and reinforced with different lattice patterns) are prepared for testing.

2.5. Testing procedure

The panels are tested in compression under displacement-controlled conditions at 0.6 mm/min using a Lloyd LR 300 kN Universal Testing Machine (UTM), with a preload of 100 N applied prior to loading. Unreinforced panels and those reinforced with conventional honeycomb lattices are also tested as benchmarks.

2.6. Results and discussion

The compressive load vs. displacement curves of auxetic LRCC (A-LRCC) panels are depicted in Fig. 6**(a)**–**(d)**, with displacement measured up to 25 mm. The mean curve of each configuration is highlighted in the graphs with a thick, red dashed line. In Fig. 6**(e)**, the averaged responses of auxetic and conventional honeycomb LRCC panels, along with that of unreinforced panels, are presented for comparison. As seen, the compressive load-displacement curves of LRCC panels consist of two distinct phases: the ascending stage, during which the compressive load increases with increasing displacement, and the descending stage, where the load decreases as displacement continues to increase.

The figure illustrates that embedding polymeric lattices alone does not substantially enhance compressive properties, as the lattice geometry plays a critical role. Specifically, A-LRCC panels outperform the conventional honeycomb LRCC panels. Although the conventional honeycomb lattice provides cohesion to the mortar by preventing disintegration, which fairly increases the residual strength, it does not provide confinement to the core mortar. Consequently, in the post-peak regime, the LRCC-C panels exhibit improved performance compared to unreinforced panels but remain notably inferior to the A-LRCC panels. The response parameters including initial stiffness (K_e), peak load (P), vertical displacement at the peak load (δ_P), residual strength ($f\,^{D}_{X}$), toughness ($T\,^{D}_{X}$), and ductility ratio (μ) determined according to (1), are extracted from the test load-displacement curves and provided in Table 3.

For the unreinforced specimens, the load rapidly drops to approximately 10 % of the peak value, and the tests are terminated due to extensive failure. Extending the displacement further for the calculation of residual strength and toughness (e.g., up to 25 mm as used for the reinforced specimens) has little effect on those values. Fig. 7 illustrates the variation in the values of the response parameters for the LRCC panels compared with the unreinforced specimens. Overall, as seen in Figs. 6 and 7 and Table 3, the embedment of auxetic lattices enhances the compressive characteristics of mortar panels, likely due to the negative Poisson's ratio (auxeticity) inducing lateral confinement under compression. The extent of this enhancement varies with lattice geometry and is examined in the following discussions.

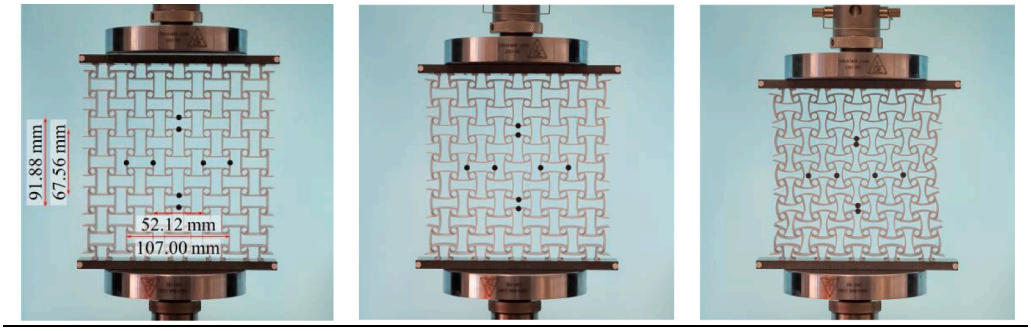

(i) Unloaded **(ii)** 10 mm **(iii)** 25 mm

(a) Tetra-anti-chiral lattice at different vertical displacement

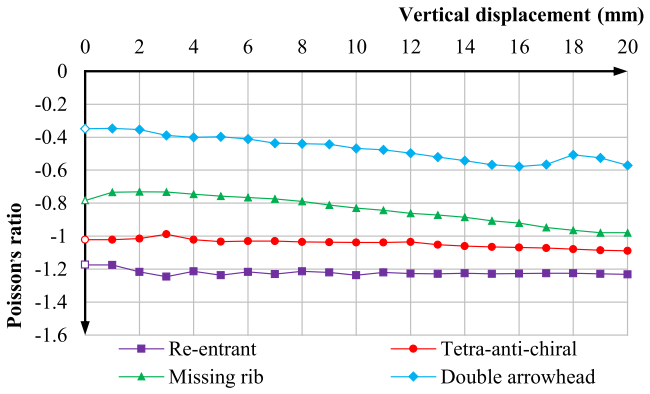

(b) Variations of Poisson's ratio against the vertical displacement

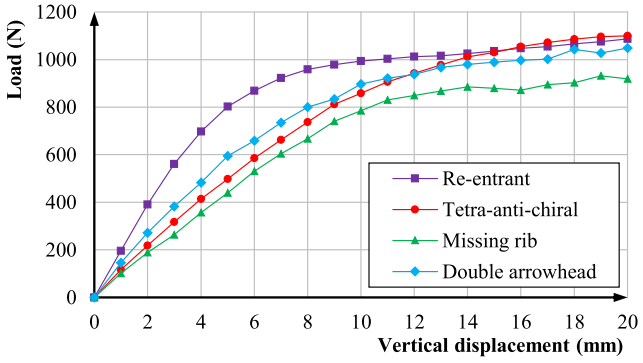

(c) Load-displacement responses

Fig. 4. Testing of auxetic lattices.

2.6.1. Initial stiffness

The initial stiffnesses of the plain and LRCC panels are calculated within the displacement ranges of 0–0.25 mm and 0–1 mm, respectively, where all the panels exhibit linear behaviour. The unreinforced panels are made of a single solid piece of mortar, whereas the LRCC panels are composed of mortar blocks connected by polymeric lattices, which have noticeable lower stiffness compared to the mortar. The confining pressure due to the lateral shrinkage tendency of the auxetic lattices depends on the Poisson's ratio of the lattice structures (negatively correlated) (see Fig. 1 and Fig. 4**(b)**) and the vertical displacement (positively correlated). Under compression, the unreinforced panels behave as a single unit until failure. Test observations show that, in contrast, the LRCC panels display relative movement between the constituent mortar blocks within each lattice cell from the early stages of loading. This movement becomes progressively restricted as vertical displacement increases and confining pressure develops (although the effect diminishes once crushing of the mortar occurs). By comparison, the conventional honeycomb LRCC panels show no noticeable confining effect.

As a result, the plain mortar panels exhibit the highest stiffness, while the panels reinforced with the non-auxetic lattice display the lowest stiffness among all the tested panels (see Table 3). Among the auxetic LRCC (A-LRCC) panels, those reinforced with the re-entrant lattice exhibit the highest stiffness, followed by the tetra-anti-chiral, missing rib, and double arrowhead lattices. This trend aligns with the Poisson's ratios of the lattices, with the re-entrant lattice having the most negative Poisson's ratio, followed by the others in the same order (see Fig. 4**(b)**). As seen in Fig. 7, the reduction in stiffness of the LRCC panels relative to the plain panels varies across the different lattice structures, with the re-entrant lattice showing the least reduction at 16.2 %, followed by the

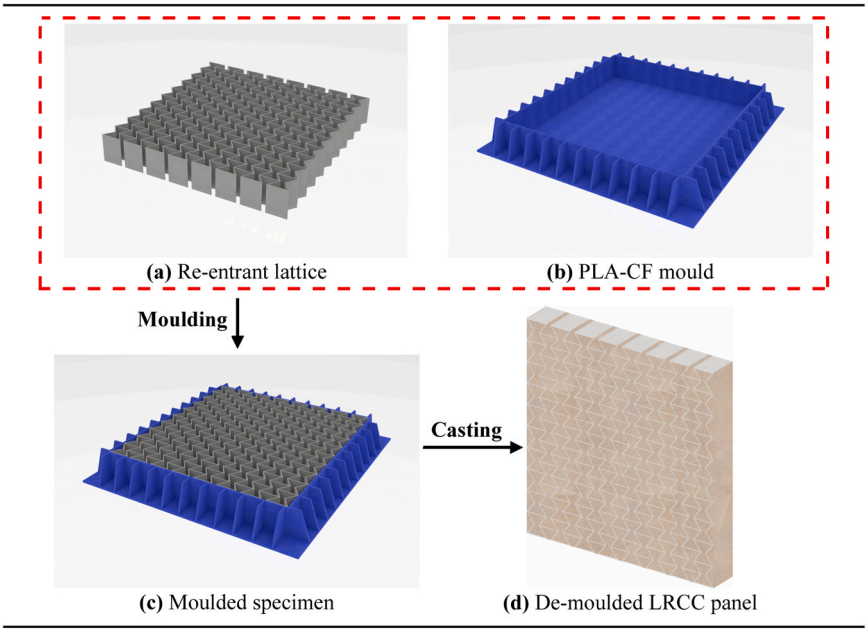

Fig. 5. Preparation of lattice reinforced mortar specimens.

tetra-anti-chiral at 44.9 %, the missing rib at 46.8 %, and the double arrowhead at 59.6 %, on average. The conventional honeycomb lattice exhibits the greatest reduction in stiffness, with a decrease of 72.7 %.

2.6.2. Peak compressive load and the corresponding displacement

The embedment of auxetic lattices in the mortar panels can enhance the peak compressive load and the corresponding displacement. As seen in Fig. 7, reinforcing mortar panels with re-entrant, tetra-anti-chiral, and double arrowhead lattices enhances the peak load of panels, on average, by 23.2 %, 17.6 %, and 10.3 % respectively, compared to their plain counterparts. However, the missing rib lattice reinforcement reduces the peak load of the mortar panels by an average of 15.4 %. This reduction may be attributed to the asymmetric geometry (about the vertical axis) of the missing-rib lattice, which exhibits a tendency to buckle laterally under compression, as observed during the lattice-only tests conducted to evaluate Poisson's ratios (see Section 2.2).

Although the filling mortar minimises the visible effects of lateral buckling in the reinforced panels, such deformation may contribute to some degree of stress redistribution across the cross-section and, in turn, to the observed reduction in peak load. Other factors, such as stress concentrations within the mortar, may also play a role and cannot be fully excluded.

The auxetic lattice reinforcement drastically enhances the displacement at peak loads, with the double arrowhead lattice improving by an average of 531.9 %, followed by the re-entrant at 491.2 %, the missing rib at 465.9 %, and finally the tetra-anti-chiral at 359.3 %. (see Fig. 7). As the conventional honeycomb lattice lacks auxeticity, it does not exert confining pressure on the mortar and, therefore, does not influence the peak load. According to Fig. 7, reinforcing panels with the conventional honeycomb lattice results in a slight reduction of 3.6 % in the peak load but a major enhancement of 394.5 % in the corresponding displacement.

2.6.3. Residual strength, toughness, and ductility ratios

Reinforcing polymeric 3D-printed lattices, whether auxetic or non-auxetic, enhances the integrity of the panels as the mortar begins to fail, resulting in improved residual strength, toughness, and ductility compared to those of the plain panels. This enhancement is particularly significant with auxetic lattices as they not only hold the mortar in place but also exert confining pressure on it, greatly amplifying the compressive performance of the panels.

According to the testing results, the re-entrant, tetra-anti-chiral, missing rib, and double arrowhead auxetic LRCC panels demonstrate substantial improvements in both residual strength and toughness, with increases of 530.2 % and 1462.6 %, 640.8 % and 1427.1 %, 542.0 % and 1112.7 %, and 797.1 % and 1504.2 %, respectively, compared to those of the plain counterparts. In contrast, the conventional honeycomb LRCC panels show relatively modest improvements of 189.8.0 % in residual strength and 763.6 % in toughness (see Fig. 7). The ductility ratio (μ) of all panels, as provided in Table 3, is calculated using Eq. (1):

$$\mu = \frac{\text{Ultimate deflection } (\Delta_u)}{\text{Elastic deflection } (\Delta_y)} \quad (1)$$

The ultimate displacement (Δ_u) is the point where the load decreases by 20 % from its peak value (L_p). The yield displacement (Δ_y) is determined from the yield point of an equivalent bilinear response curve, constructed such that the area under the bilinear curve is equal to that of the actual load-displacement curve (see Fig. 8).

As seen in Fig. 7, the ductility ratios of the auxetic LRCC panels exhibit notable improvements over the plain panels. The missing rib LRCC panels show the highest increase in ductility at 264.5 %, followed by the re-entrant LRCC panels with an improvement of 172.5 % and the tetra-anti-chiral LRCC panels with 147.8 %. In contrast, the double arrowhead LRCC panels exhibit a more moderate improvement of 103.6 %, while the non-auxetic conventional honeycomb LRCC panels display only a slight increase of 24.64 % in ductility, further highlighting the superior contribution of the auxetic lattices in enhancing the mechanical properties of mortar panels.

2.6.4. Failure pattern

The failure behaviour of the LRCC specimens in this study is characterised by the formation of an "X" type shear failure pattern across all LRCC specimens, irrespective of the lattice geometry, as seen in Fig. 9.

This pattern involves diagonal cracks intersecting to form an "X" shape, which typically occurs due to shear stresses that develop under compressive or bending loads. The embedded lattices play a significant role in this failure mode by redistributing stresses and confining the mortar, preventing sudden brittle fracture. As the load increases, stress concentration near the lattice nodes promotes crack initiation, which then propagates diagonally due to the shear forces, ultimately forming

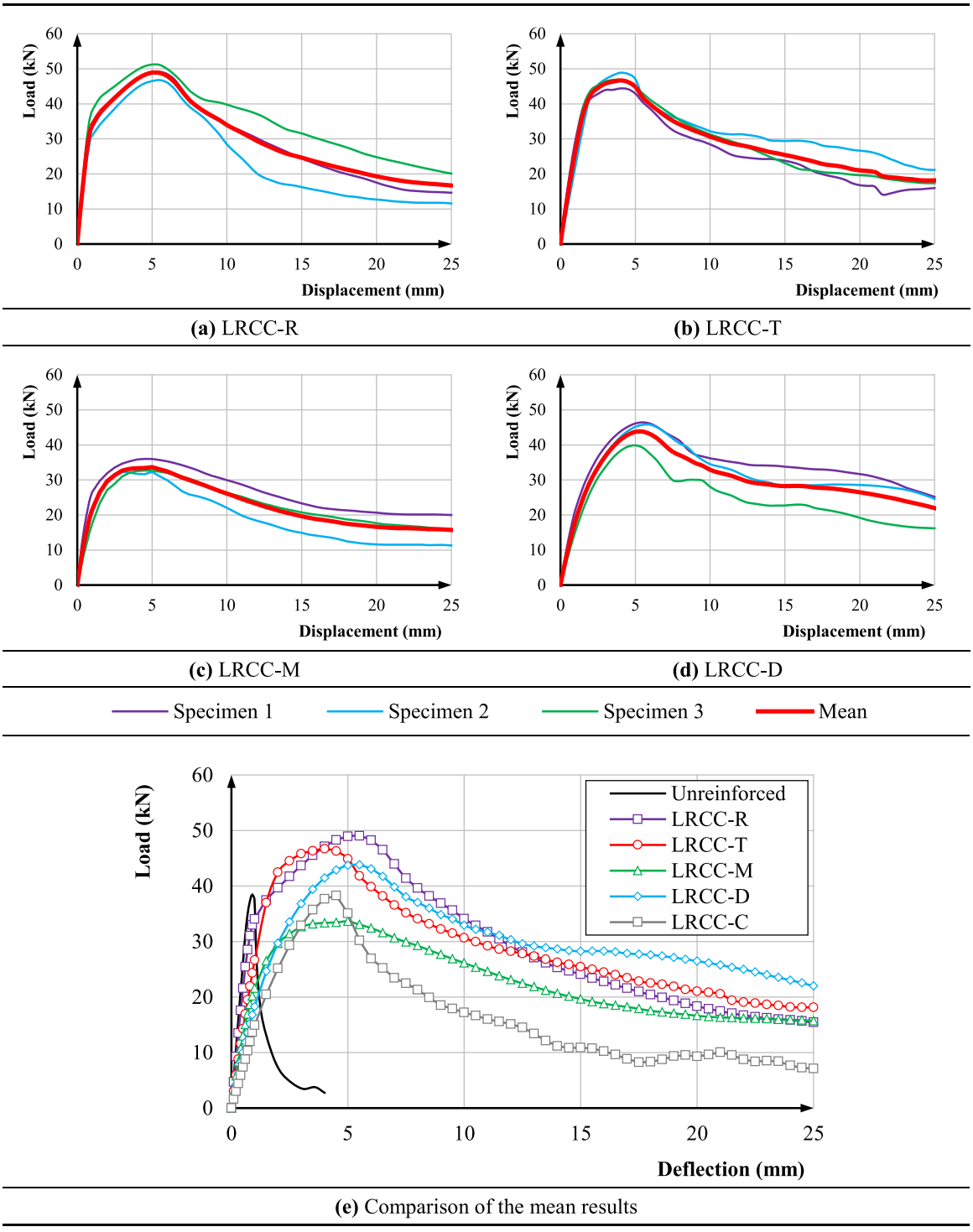

Fig. 6. Compressive load-displacement of panels.

the "X" pattern. This failure mode demonstrates the ability of the embedded lattices to control crack propagation and enhance the ductility of the panels by maintaining their structural integrity even under severe loading conditions.

2.7. Experimental testing remarks

Findings of the compression testing on the mortar-filled polymeric lattices are summarised as follows:

1. The reinforcing polymeric lattices (auxetic or non-auxetic) generally improves the compressive characteristics of mortar panels, with enhancements ranging from slight to drastic depending on the lattice structure, albeit with compromised initial stiffness.
2. The auxetic LRCC panels outperform the conventional honeycomb LRCC panels due to their negative Poisson's ratio (NPR) and the consequent confinement effect.
3. The re-entrant LRCC panels demonstrate the highest enhancement in peak load, while the missing rib counterparts exhibit the greatest improvement in ductility ratio. The remaining studied parameters, i.

Table 3
Testing results of unreinforced and lattice-reinforced specimens.

Specimen Type	Specimen No.	K_e (kN/mm)	P (kN)	δ_P (mm)	f_X^{D*} (kN)	T_X^{D*} (kN.mm)	μ (-)
Unreinforced	1	52.77	39.0	1.03	2.04	47.06	1.35
	2	54.29	43.1	0.95	4.29	51.69	1.22
	3	55.82	42.7	0.81	1.03	42.10	1.24
	Mean	**54.29**	**39.7**	**0.91**	**2.45**	**46.95**	**1.38**
LRCC-R	1	33.08	49.1	5.53	14.63	728.14	3.48
	2	30.93	46.5	5.54	11.57	609.10	3.20
	3	38.07	51.2	5.15	20.11	863.69	4.54
	Mean	**34.03**	**48.9**	**5.38**	**15.44**	**733.65**	**3.76**
LRCC-T	1	29.65	44.4	4.22	15.96	658.32	4.03
	2	22.17	48.9	4.03	21.14	784.27	2.62
	3	28.07	46.8	3.54	17.35	708.37	3.91
	Mean	**26.62**	**46.7**	**4.18**	**18.15**	**716.99**	**3.42**
LRCC-M	1	26.55	36.0	4.52	20.01	658.50	6.51
	2	20.61	32.3	5.08	11.29	478.11	4.34
	3	17.56	32.7	4.5	15.89	571.52	4.45
	Mean	**21.57**	**33.6**	**5.15**	**15.73**	**569.37**	**5.03**
LRCC-D	1	21.56	46.4	5.56	25.17	852.87	3.02
	2	17.87	45.8	6.35	24.59	792.45	2.70
	3	15.35	39.9	5.65	16.19	614.21	2.21
	Mean	**18.26**	**43.8**	**5.75**	**21.98**	**753.18**	**2.81**
LRCC-C	1	14.41	39.63	4.53	8.41	384.03	1.63
	2	15.90	37.23	4.15	4.40	373.97	1.68
	3	14.47	39.83	4.56	8.49	458.34	1.64
	Mean	**14.93**	**38.28**	**4.50**	**7.10**	**405.45**	**1.72**

* $X = 4$ mm for unreinforced specimens and 25 mm for reinforced specimens.

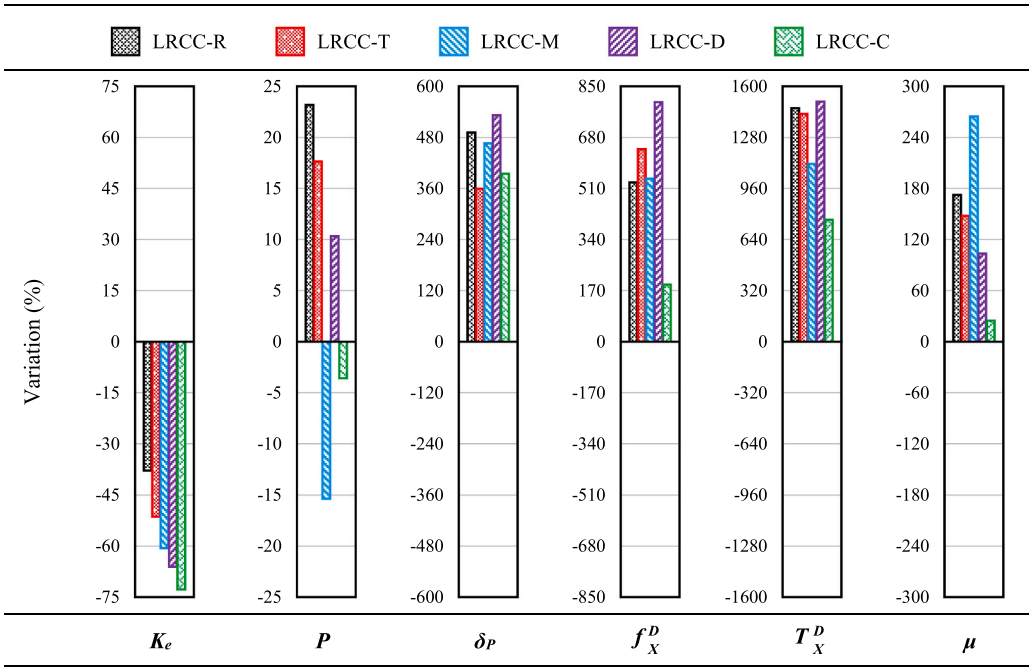

Fig. 7. Effects of different lattice reinforcement on compressive performance.

e. displacement at peak load, residual strength, and toughness, are highest for the tetra-anti-chiral LRCC specimens.

These findings underscore the adaptability of lattice reinforcement in enhancing compressive characteristics including ductility, and energy absorption of cementitious composites.

3. Numerical modelling and validation

The mean compressive stress-strain behaviour of the plain mortar cubes serves as the constituent stress-strain input for the FE modelling of the mortar material. The mortar is represented using the Concrete Damage Plasticity (CDP) model in ABAQUS/Explicit dynamic analysis [20,21]. The CDP model, an adaptation of the Drucker-Prager hypothesis, integrates yield and failure criteria alongside a flow rule to effectively simulate the plasticity and damage behaviour of brittle cementitious materials such as mortar. It assumes that the failure surface in the deviatoric cross-section, as determined from triaxial stress experiments on cylindrical specimens, is not circular. This surface is defined by the parameter K, which represents the ratio between the distance from the hydrostatic axis to the compression axis (CA), denoted as a, and the distance from the hydrostatic axis to the tension axis (TA), denoted as b, as defined in Eq. (2). The CA corresponds to the principal compression stress direction, while the TA represents the principal

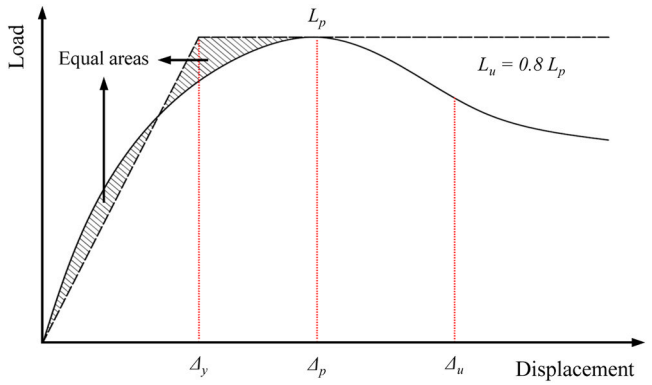

Fig. 8. Method for computing ductility ratio from load-displacement curves.

tension stress direction in the deviatoric plane. Previous studies recommend a range of 0.60–0.67 for the K parameter (see Fig. 10) [22].

$$K = \frac{a}{b} \tag{2}$$

Assuming the mortar is subjected to high confining pressure, the flow potential (G) and yield surface can be defined using the non-associated Drucker-Prager hyperbolic function, as shown in Eq. (3).

$$G = \sqrt{(\epsilon . f_{to} . \tan\psi)^2 + q^2} - p . \tan\psi \tag{3}$$

Where, p represents the hydrostatic pressure stress, q is the Mises equivalent effective stress, and ψ is the dilation angle, measured in the p-q plane at high confining pressure. This angle, lying between the hydrostatic axis and the yield function, indicates the material's volume change under shear which ranges from zero to the friction angle [23]. The parameter f_{to} denotes the uniaxial tensile stress at failure, and ϵ is the eccentricity parameter, defining the rate at which G approaches its asymptote (as ϵ approaches zero, the flow potential approaches a straight line) [24]. The stress-strain relationship of mortar is then described by the CDP model stress-strain equation (see Eq. (4)).

$$\sigma = (1 - d_n) E_o (\varepsilon - \varepsilon^{pl}) \tag{4}$$

Where, σ represents the Cauchy stress, E_o is the initial Young's modulus of the material, ε is the total strain, and ε^{pl} is the plastic strain. Besides, the d_n parameter is a non-dimensional damage parameter ranging from 0 to 1 such that at 0, no damage or degradation of the elastic modulus occurs, while $d_n = 1$ indicates complete destruction (i.e., full degradation of Young's modulus) of the material. For the mortar in compression, Ritter's parabola (Eq. (5)) is used to model the ascending portion of the uniaxial stress-strain relationship, with a simplified constant slope for the post-peak curve (Eq. (6)). The damage parameter is defined according to Eq. (7).

$$0 < \varepsilon_c < \varepsilon_o' : \qquad \frac{f_c}{f_{cu}} = 2\frac{\varepsilon_c}{\varepsilon_o'}\left(1 - \frac{\varepsilon_c}{2\varepsilon_o'}\right) \tag{5}$$

$$\varepsilon_o' < \varepsilon_c < \varepsilon_{cu} : \qquad \frac{f_c}{f_{cu}} = 1 - 0.15\left(\frac{\varepsilon_c - \varepsilon_o'}{\varepsilon_{cu} - \varepsilon_o'}\right) \tag{6}$$

$$d_c = 1 - \frac{f_c}{f_{cu}} \tag{7}$$

Where, ε_c is compressive strain, f_{cu} is the uniaxial compressive strength, ε_{cu} is the ultimate compressive strain, $\varepsilon_o{}'$ is the strain at the peak stress (f_{cu}), and d_c is the damage parameter in uniaxial compression. For the uniaxial tensile behaviour of the mortar, Eqs. (8)–(10) are used to obtain the stress-strain relationship of the CDP model, as seen in Table 4.

$$\varepsilon_t \le \varepsilon_{cr} : \qquad f_t = E_o \varepsilon_t \tag{8}$$

$$\varepsilon_t \ge \varepsilon_{cr} : \qquad \frac{f_t}{f_{tu}} = \left(\frac{\varepsilon_{cr}}{\varepsilon_t}\right)^n \tag{9}$$

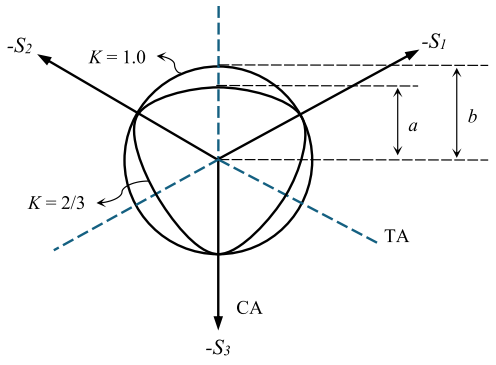

Fig. 10. Deviatoric cross-section.

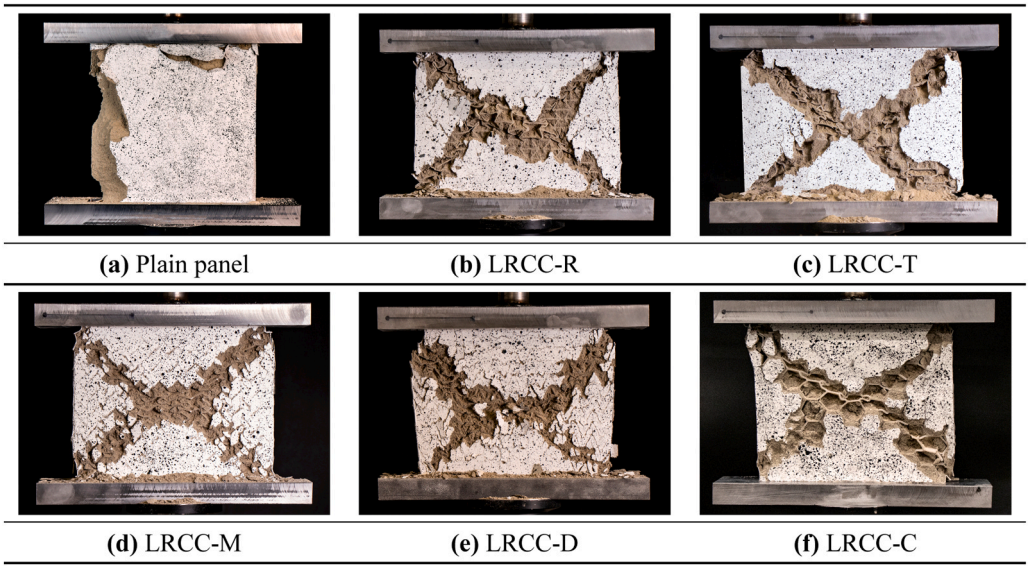

Fig. 9. Failure pattern of panels under compression.

Table 4
Compressive and tensile stress-strain data for mortar CDP model.

Uniaxial compression data			Uniaxial tension data		
Comp. stress f_c: MPa	Inelastic strain ε^{in}: -	Damage parameter d_c: -	Tensile stress f_t: MPa	Inelastic strain ε^{in}: -	Damage parameter d_t: -
6.00	0.0000	0.0000	0.60	0.0000	0.0000
5.98	0.0014	0.0051	0.46	0.0002	0.2270
5.95	0.0016	0.0108	0.36	0.0004	0.4033
5.86	0.0020	0.0266	0.28	0.0007	0.5393
5.52	0.0031	0.0837	0.21	0.0009	0.6444
5.10	0.0042	0.1551	0.16	0.0011	0.7255
4.62	0.0053	0.2344	0.13	0.0013	0.7881
4.12	0.0064	0.3185	0.10	0.0015	0.8364
3.59	0.0075	0.4058	0.08	0.0017	0.8737
3.06	0.0086	0.4952	0.06	0.0019	0.9025
2.57	0.0096	0.5757			
2.20	0.0107	0.6382			
1.90	0.0118	0.6877			
1.46	0.0138	0.7604			
1.16	0.0158	0.8103			
0.94	0.0179	0.8460			
0.78	0.0198	0.8725			
0.56	0.0238	0.9084			

$$d_t = 1 - \frac{f_t}{f_{tu}} \tag{10}$$

Where, ε_t and ε_{cr} are the tensile and cracking strains respectively, f_t and f_{tu} are the tensile and maximum tensile stresses respectively, d_t is the damage parameter in uniaxial tension and n is a calibration parameter taken as 0.4. Moreover, Eqs. (5)–(7) are calibrated with the experimental compressive stress-strain data while Eqs. (8)–(10) are used to establish the tensile stress-strain relationship with f_{tu} taken as 10 % of f_{cu}, as provided in Table 4.

The parameters of CDP model, including the dilation angle (ψ), flow potential eccentricity (ϵ), ratio of biaxial to uniaxial compressive strength (f_{bo} / f_{co}), and ratio of the stress invariant on the tensile meridian (K) are set to 37°, 0.1, 1.16, and 0.67, respectively. The mortar density is assumed to be 2300 kg/m^3.

Although PETG is inherently isotropic, the 3D printing process introduces anisotropy, resulting in comparable mechanical properties within the print layers (through depth and thickness) and distinct properties along the print direction. The elastic behaviour is modelled using orthotropic elasticity, with a Young's modulus of 1.875×10^3 MPa assigned for the directions along the depth and thickness and 1.900×10^3 MPa for the print direction, as determined from tensile dog-bone testing (see Fig. 3). The Poisson's ratios in all three directions are assumed to be equal, with a value of 0.4. The stress-strain curves, as shown in Fig. 3, are utilised to characterise the nonlinear behaviour of the printed PETG material. An orthotropic hardening plasticity model is adopted, with yield stresses specified as 30.8 MPa for the directions along the depth and thickness and 43.5 MPa for the print direction. Additionally, a ductile damage model is incorporated to simulate the progressive material degradation, capturing early failure along the depth due to weak interlayer adhesion. The failure model utilises a maximum principal strain criterion, ensuring that the material's stiffness in the weak directions reduces to zero upon reaching the critical strain, while no failure is modelled in the print direction due to PETG's high fracture strain and resistance to rupture. The PETG density is assumed to be 1250 kg/m^3. This material constituent model effectively represents the anisotropic and failure behaviour of 3D-printed PETG in the FE simulations.

Both the lattices and the mortar are simulated using solid elements with reduced integration (C3D8R). The lattices and the mortar are modelled as solid elements, assembled into a 3D entity, with the volume of concrete where the panel resides subsequently removed. This process creates a surface-to-surface contact between the concrete and the lattice, with the interaction defined by a coefficient of friction (μ_f). The lattices and the mortar are meshed using a hexagonal pattern.

A mesh sensitivity analysis is conducted with a series of compression simulations up to 4 mm displacement on all panel configurations, showing that refining the mesh below 4 mm for the mortar and 1 mm for the lattice produces negligible changes in the load-displacement response. During the full simulations (compression up to 25 mm), the element size is further refined when necessary to overcome convergence difficulties, particularly for the LRCC-D and LRCC-M configurations.

The lattice-mortar interface is modelled with hard contact in the normal direction (no penetration, separation allowed) and frictional behaviour in the tangential direction. This ensures full load transfer under compression while allowing local slip. The hard contact governs the confinement effect, and the friction controls shear transfer, directly influencing stiffness and failure mechanisms of the composite. A parametric study is performed on the re-entrant LRCC panel to evaluate the effect of the PETG lattice-mortar interface coefficient of friction, considering values of 0.3, 0.4, 0.5, 0.6, and 0.7. It is shown that variations in the friction coefficient have minimal effect on the overall load-displacement trend, though they shift the load levels; this offset is most pronounced at small displacements and diminishes as displacement increases (see Fig. 11).

The FE simulations indicate that a friction coefficient of 0.5 consistently gives the best overall agreement with the experimental load-displacement responses across all PETG LRCC panel types and is therefore adopted in the models (see Fig. 12). The failure patterns predicted by the FE models is shown in Fig. 13. The initial stiffness (K_e), peak load (P), and toughness ($T\frac{D}{X}$) of the FE models are compared with the experimental results, as shown in Table 5. As observed, the experimental and numerical results demonstrate reasonable agreement, which validates the model for further exploration of such a composite system.

3.1. Steel lattice-reinforced concrete panels

In the experimental phase, PETG is used for the lattice due to its ease of 3D printing and geometric accuracy. While PETG and mortar are not common in structural applications, they provide a practical way to validate the concept, with the promising experimental results confirming its viability. To align with practical applications, in the validated numerical models, the materials used (mortar and PETG) are substituted with conventional construction materials, i.e. normal-strength concrete (f_{cu} = 40 MPa) and steel (f_y = 386 MPa). Fig. 14 shows the stress-strain curves of the concrete and steel used in the numerical simulations. The concrete is modelled using the Concrete Damage Plasticity (CDP) model in Abaqus [20,21], while the steel is modelled using metal plasticity with isotropic hardening. These constitutive laws capture the nonlinear behaviour of both materials. The lattice geometries and reinforcement ratios are kept constant with those of the PETG-LRCC panels.

The compressive response of the concrete panels reinforced with

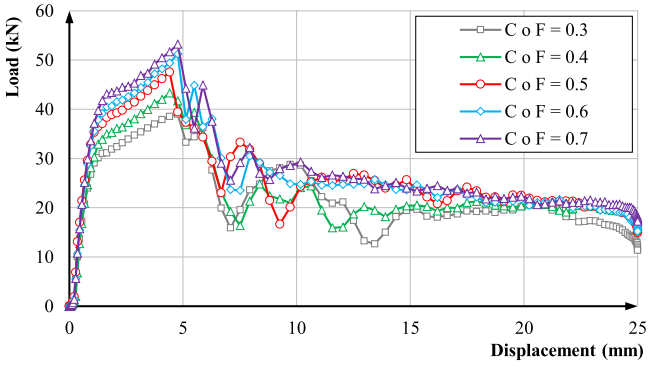

Fig. 11. Effect of friction coefficient on compressive response of LRCC-R.

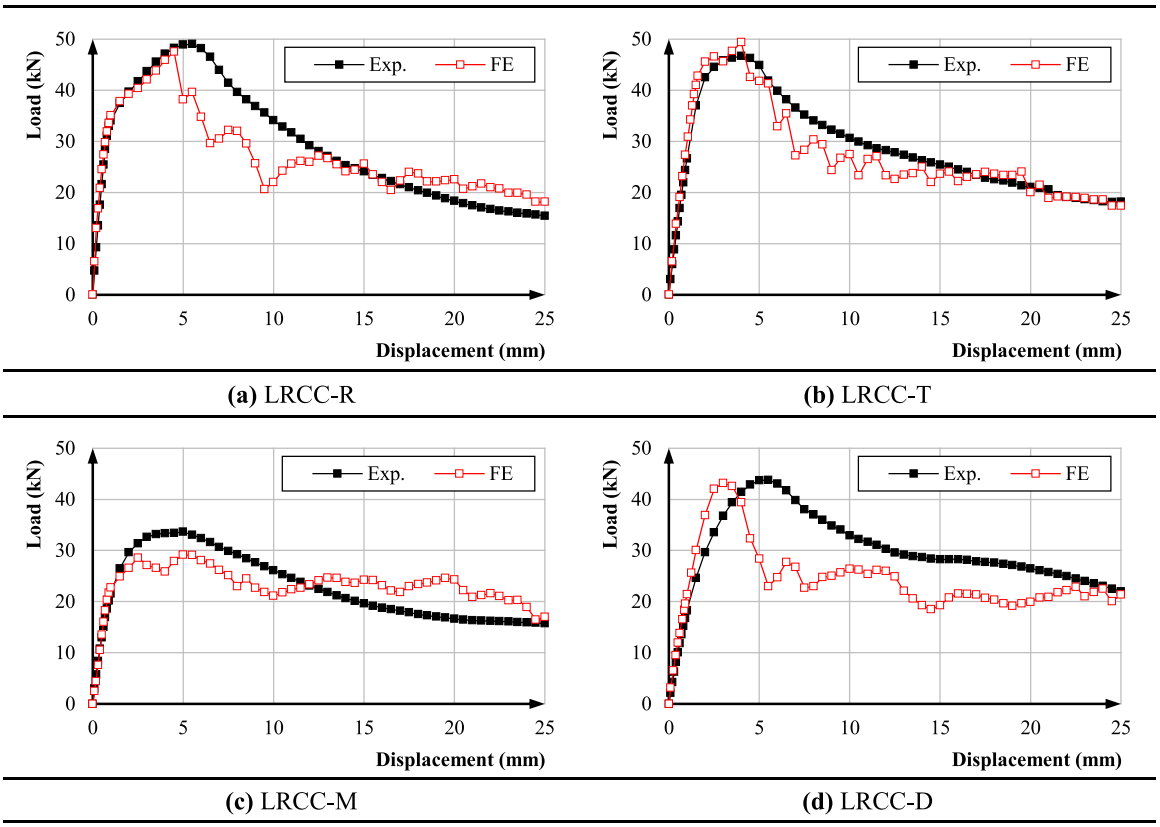

Fig. 12. Compressive load-displacement of FE models vs. their experimental counterparts.

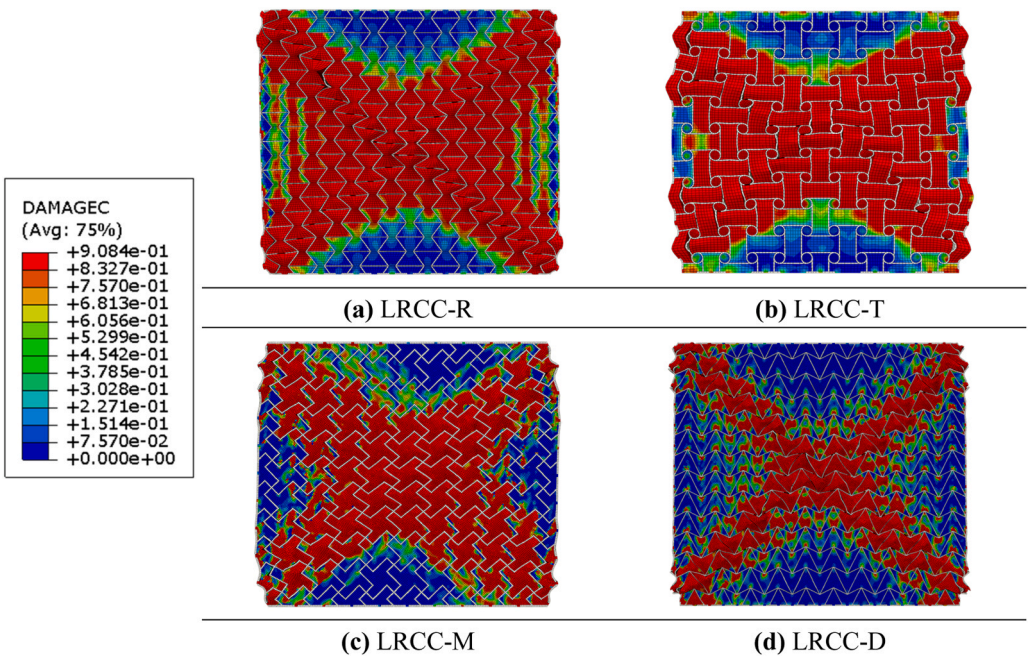

Fig. 13. Failure pattern of FE models at 10 mm vertical displacements. (red indicates total compressive failure, blue denotes no failure).

steel re-entrant, tetra-anti-chiral, missing rib, double arrowhead and conventional honeycomb lattices are presented in Fig. 15. As observed, the incorporation of a steel auxetic lattice significantly enhances the compressive behaviour of concrete panels, promoting a hardening response. Due to the ductility and high failure strain capacity of steel, this enhancement persists even at large deformations, extending up to a displacement of 25 mm. The compression performance of steel A-LRCC panels exhibits an initial linear phase up to the elastic limit load, followed by a sudden load drop. According to the FE simulation, this drop corresponds to the onset of concrete failure. The load then increases again as the lattice begins to impose lateral confinement on the concrete panel, enhancing its resistance. As expected, the missing rib lattice-

Table 5
Comparison of experimental results and numerical predictions.

Parameters	K_e (kN/mm)			P (kN)			T_X^D (kN.mm)		
Specimens	**Exp.**	**FE**	**Exp./FE**	**Exp.**	**FE**	**Exp./FE**	**Exp.**	**FE**	**Exp./FE**
LRCC-R	34.03	35.04	0.97	48.9	47.6	1.03	733.65	682.91	1.07
LRCC-T	26.62	29.42	0.90	46.7	49.4	0.95	716.99	681.26	1.05
LRCC-M	21.57	22.77	0.95	33.6	29.1	1.15	569.37	581.97	0.98
LRCC-D	18.26	21.42	0.85	43.8	43.2	1.01	753.18	607.94	1.24

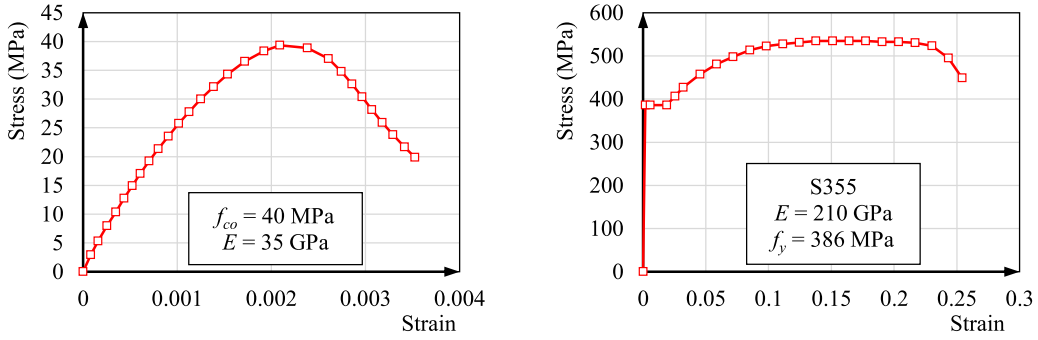

Fig. 14. Stress-strain curve for concrete (compressive) and steel (tensile).

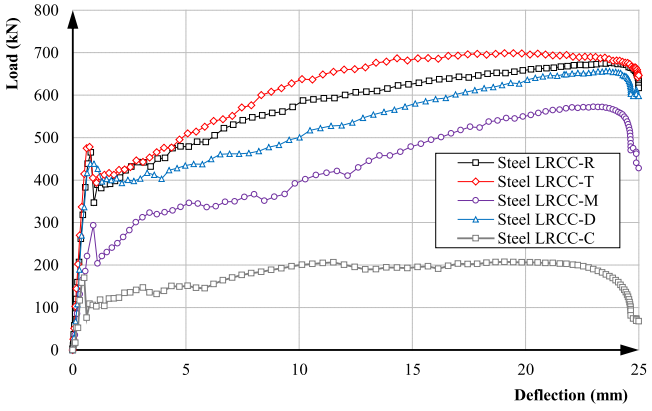

Fig. 15. Compressive behaviour of steel lattice-reinforced concrete panels: FE models.

reinforced concrete model exhibits inferior performance compared to the other panels due to its tendency for lateral buckling, while the other three panels demonstrate comparable performance.

The concrete panel reinforced with a conventional honeycomb lattice, which lacks auxeticity, exhibits significantly inferior performance compared to panels reinforced with steel auxetic lattices. Due to the absence of auxetic behaviour, the honeycomb lattice is unable to impose confining pressure on the concrete. Consequently, once the concrete panel reaches its first peak load and begins to fail, there is no significant restraining force to sustain its load-bearing capacity. As a result, a load plateau occurs, where the load remains relatively constant over an increasing displacement range before further degradation.

By comparison, while PETG is relatively flexible and ductile along the print direction, its interlayer bonding is significantly weaker and prone to sudden failure in the transverse direction. Consequently, in the PETG-LRCC panels, both the experimental observations and FE results indicate that the lattice walls aligned through the depth are susceptible to interlayer debonding and premature fracture. This mechanism prevents the development of a sustained confinement effect, leading to softening rather than hardening in the post-peak regime.

As a point of reference, Zhong et al. [12] examined concrete composites with auxetic aluminium honeycomb lattices (aluminium with f_y = 274 MPa and E = 69 GPa; concrete with f_{cu} = 16.5 MPa and E = 8 GPa; reinforcement ratio = 0.2 %). The specimens demonstrated a three-stage response with a stable post-peak plateau due to confinement. In contrast, the FE models of steel-concrete LRCC panels in this study (steel with f_y = 386 MPa and E = 210 GPa; concrete with f_{cu} = 40 MPa and E = 35 GPa; reinforcement ratio = 15 %) exhibit post-peak hardening. This difference might arise from the substantially higher reinforcement ratio and the stronger lattice material, yet both studies confirm that ductile metallic lattices (aluminium or steel) sustain confinement at large displacements, unlike PETG lattices which suffer interlayer debonding and sudden fracture.

3.2. *Numerical simulation remarks*

The FE model provides a reliable representation of the compressive behaviour of PETG lattice-reinforced mortar panels. The same modelling approach has subsequently been used to simulate the compressive behaviour of steel auxetic LRCC panels, which demonstrate a hardening response trend in contrast to the PETG counterparts. However, as noted in Section 3, the nonlinear parameters, particularly the key interaction parameters, must be carefully calibrated against relevant experimental data in the future to ensure reliability.

The model can serve as a virtual laboratory unit for simulating and investigating the performance of different structural elements, such as columns and beams reinforced with auxetic lattices. The model can also enable optimisation studies, allowing for the exploration of lattice geometries, material combinations, and reinforcement strategies to improve structural efficiency and performance. While it provides useful initial insights, its reliability is limited, and further validations under various scenarios are necessary to ensure accurate predictions.

4. Conclusions

This study investigates the structural behaviour of lattice-reinforced cementitious composite (LRCC) panels through experimental testing and numerical simulations. The experimental phase employs PETG lattices embedded in mortar, selected for their ease of fabrication and geometric precision, to validate the feasibility of the concept. The results demonstrate that incorporating lattice reinforcement significantly enhance the compressive response of the panels, particularly in terms of stiffness,

peak load, residual strength, and toughness.

Building on these experimental findings, an FE model is developed and refined by replacing PETG and mortar with conventional construction materials (steel and normal-strength concrete) to align with practical engineering applications. The numerical simulations provide deeper insights into the confinement effects introduced by auxetic lattices, underscoring their potential to enhance structural performance.

Overall, this research confirms the viability of lattice-reinforced composites and demonstrates that the auxetic nature of embedded lattices enhances ductility, toughness and possible slight enhancement in peak load of panels through their confinement effect. The transition from PETG-mortar to steel-concrete in the numerical model helps bridge experimental validation and real-world application, providing a basis for further study. In structural applications where greater ductility, damage tolerance, and post-peak load retention are required, auxetic lattice reinforcement offers an efficient confinement-based solution; however, further research on normal-strength concrete, scale effects, and dynamic loading is needed to support broader adoption.

CRediT authorship contribution statement

John J. Orr: Resources, Project administration, Methodology, Funding acquisition. **Ken E. Evans:** Supervision, Methodology, Investigation, Funding acquisition. **Prakash Kripakaran:** Writing – review & editing, Supervision, Resources, Project administration, Methodology, Investigation, Funding acquisition. **Raffaele Vinai:** Writing – review & editing, Supervision, Resources, Project administration, Methodology, Investigation, Funding acquisition. **Amila Jayasinghe:** Visualization, Validation, Methodology. **Owoichoechi Momoh Emmanuel:** Validation, Methodology, Formal analysis. **Liyao Wan:** Writing – review & editing, Validation, Software. **Mohammad Hajsadeghi:** Writing – review & editing, Writing – original draft, Methodology, Investigation, Formal analysis, Data curation, Conceptualization.

Declaration of Competing Interest

The authors declare that they have no known competing financial interests or personal relationships that could have appeared to influence the work reported in this paper.

Acknowledgements

This work was supported by the United Kingdom's Engineering and Physical Sciences Research Council (EPSRC, UK), [EP/W019027/1].

Appendix A. Supporting information

Supplementary data associated with this article can be found in the online version at doi:10.1016/j.conbuildmat.2025.144585.

Data availability

Data will be made available on request.

References

[1] K.E. Evans, M.A. Nkansah, I.J. Hutchinson, S.C. Rogers, Molecular network design, Nature 353 (1991) 124.
[2] E.M. Momoh, A. Jayasinghe, M. Hajsadeghi, R. Vinai, P. Kripakaran, K.E. Evans, J. Orr, A state-of-the-art review on the application of auxetic materials in cementitious composites, Thin-Walled Struct. 196 (2024) 111447.
[3] A. Bentur, S. Mindess. Fibre Reinforced Cementitious Composites, 2nd ed., Taylor & Francis, London, 2007.
[4] P. Balaguru, S.P. Shah, Fiber-Reinforced Cement Composites, McGraw-Hill, New York, 1992.
[5] S. Spadea, I. Farina, A. Carrafiello, F. Fraternali, Recycled nylon fibers as cement mortar reinforcement, Compos. Part B Eng. 80 (2015) 117–123.
[6] G. Fischer, V.C. Li, Effect of fiber reinforcement on the response of structural members, Eng. Fract. Mech. 74 (2007) 258–272.
[7] X.Y. Zhang, K. Lee, Performance of auxetic lattices in structures, in: Proc. 12th Int. Conf. Struct. Eng., Springer, Tokyo, Japan, 2018, pp. 45–50.
[8] B. Salazar, P. Aghdasi, I.D. Williams, C.P. Ostertag, H.K. Taylor, Polymer lattice-reinforcement for enhancing ductility of concrete, Mater. Des. 196 (2020) 109184.
[9] M. Chen, Z. Chen, Y. Xuan, T. Zhang, M. Zhang, Static and dynamic compressive behaviour of 3D printed auxetic lattice reinforced ultra-high-performance concrete, Cem. Concr. Compos. 139 (2023) 105046.
[10] W. Hao, J. Liu, H. Kanwal, Compressive properties of cementitious composites reinforced by 3D printed PA6 lattice, Polym. Test. 117 (2023) 107811.
[11] G. Tzortzinis, A. Gross, S. Gerasimidis, Auxetic boosting of confinement in mortar by 3D re-entrant truss lattices for next-generation steel-reinforced concrete members, Extrem. Mech. Lett. 52 (2022) 101681.
[12] R. Zhong, X. Ren, X.Y. Zhang, C. Luo, Y. Zhang, Y.M. Xie, Mechanical properties of concrete composites with auxetic single and layered honeycomb structures, Constr. Build. Mater. 322 (2022) 126453.
[13] H. Zhou, K. Jia, X. Wang, M.-X. Xiong, Y. Wang, Experimental and numerical investigation of low velocity impact response of foam concrete filled auxetic honeycombs, Thin-Walled Struct. 154 (2020) 106898.
[14] N.K. Choudhry, T.K. Nguyen, V. Nguyen-Van, B. Panda, P. Tran, Auxetic lattice reinforcement for tailored mechanical properties in cementitious composite: experiments and modelling, Constr. Build. Mater. 438 (2024) 137252.
[15] T. Vitalis, A. Gross, G. Tzortzinis, B. Schagen, S. Gerasimidis, Enhancing mortar composite matrices with three-dimensional auxetic truss lattice materials for reinforced concrete structures, Constr. Build. Mater. 457 (2024) 139165.
[16] A. Jayasinghe, M. Hajsadeghi, L. Wan, J. Orr, R. Vinai, P. Kripakaran, K. Evans, Design and construction of concrete shells using semi-flexible auxetic grids as formwork, Structures 80 (2025) 109833.
[17] G. Smith, L. Johnson, Influence of printing orientation on mechanical properties of 3D printed PETG lattices, Addit. Manuf. 30 (2019) 100–110.
[18] A. Brown, M. Davis, Effect of raster angle on the structural integrity of 3D printed thin-walled structures, Mater. Des. 150 (2018) 124–134.
[19] ISO 527-1:2019, Plastics – Determination of Tensile Properties – Part 1: General Principles, Int. Organ. Stand., Geneva, Switzerland, 2019.
[20] H. Chen, W. Ma, B. Kasal, Y. Wei, L. Yan, Flexural behavior of adhesively bonded cross-laminated timber-concrete composite (TCC) panel with glass-fiber textile mesh as reinforcement in concrete: experimental studying and numerical simulation, Eng. Struct. (2025) 119916.
[21] B. Neupane, K. Sahani, S.S. Khadka, Experimental testing and numerical simulation of recycled concrete aggregate in a concrete mix, Int. J. Concr. Struct. Mater. 19 (5) (2025).
[22] W. Ren, L.H. Sneed, Y. Gai, X. Kang, Test results and nonlinear analysis of RC T-beams strengthened by bonded steel plates, Int. J. Concr. Struct. Mater. 9 (2015) 133–143.
[23] T. Ozbakkaloglu, A. Gholampour, J.C. Lim, Damage-plasticity model for FRP-confined normal-strength and high-strength concrete, J. Compos. Constr. 20 (2016) 0416053.
[24] E.O. Momoh, A.I. Osofero, O. Menshykov, Behaviour of clamp-enhanced palm tendons reinforced concrete, Constr. Build. Mater. 341 (2022) 127824.